A NEW APPROACH TO IDENTIFY ON-GROUND LAMP TYPES FROM NIGHT-TIME ISS IMAGES

Natalia Rybnikova [a,b,c,*], *Alejandro Sánchez de Miguel* [d,e], *Sviatoslav Rybnikov* [f,g], *Anna Brook* [c]

[a] Dept. of Mathematics, University of Leicester, Leicester LE1 7RH, United Kingdom

[b] Dept. of Natural Resources and Environmental Management, University of Haifa, Haifa 3498838, Israel

[c] Dept. of Geography and Environmental Studies, University of Haifa, Haifa 3498838, Israel

[d] Environment and Sustainability Institute, University of Exeter, Penryn Campus, Penryn, Cornwall, TR10 9FE, United Kingdom

[e] Dept. Física de la Tierra y Astrofísica, Instituto de Física de Partículas y del COSMOS (IPARCOS), Universidad Complutense de Madrid, 28040, Madrid, Spain

[f] Institute of Evolution, University of Haifa, Haifa 3498838, Israel

[g] Dept. of Evolutionary and Environmental Biology, University of Haifa, Haifa 3498838, Israel

[*] Corresponding author. Email: nrybhiko@campus.haifa.ac.il, nataliya.rybnikova@gmail.com

Abstract: Artificial night-time light (NTL), emitted by various on-ground human activities, becomes further intensive in many regions worldwide. Its adverse effects on humans' and ecosystems' health crucially depend on the light spectrum, making the remote discrimination between different lamps a highly important task. However, such studies remain extremely limited, and none of them exploits freely available satellite imagery. In the analysis, the possibility to remotely assess the relative contribution of different lamp types into outdoor lighting is tested. For this sake, the radiometrically calibrated ISS RGB image is used. Spatial resolution of the image is ~20 meters, implying that each pixel may represent a mixture of different lamp types. Unmixing analysis to the detailed spectral signatures of the corresponding *in situ* measurements is performed, with 'pure' lamps' signatures as the endmembers. Afterwards, statistical models to reproduce the

results of unmixing based on the broad-band RGB image from the ISS are run. The built models predict well (with R^2 reaching ~0.87) the contribution of high-pressure sodium (HPS) and metal-halide (MH) lamps, the most spread in the study area (Haifa, Israel). The restored map for HPS allocation demonstrates high concordance with the network of municipal roads, while that for MH shows notable coincidence with the industrial facilities and the airport.

Keywords: RGB night-time imagery, ISS, radiometric calibration, *in situ* measurement, lamp type, unmixing.

1. Introduction

Artificial night-time light (NTL), emitted by various on-ground human activities, becomes further intensive in many countries, making the world brighter (Cinzano et al., 2001; Falchi et al., 2016; Kyba et al., 2017; Zheng et al., 2021). At the same time, a huge amount of empirical evidence has been accumulated for adverse effects of NTL on both humans (Garcia-Saenz et al., 2018; Haim and Portnov, 2013; Kloog et al., 2009; McFadden et al., 2014) and ecosystems (Gaston et al., 2013; Hölker et al., 2010; Longcore et al., 2004; Owens et al., 2020). An especially serious concern comes from the long-term cumulative effects of NTL, which remains almost unexplored (Lyytimäki, 2015). Besides, NTL also embarrasses professional astronomical observations (Kyba, 2018; Riegel, 1973; Zhang et al., 2017). With respect to the above-mentioned challenges, the necessity to regulate light pollution becomes further more recognized (Cho et al., 2011; Falchi and Bará, 2020; Morgan-Taylor, 2015).

The adverse effects of NTL are known to depend crucially on the light spectrum (Brainard et al., 2001; Gaston et al., 2014; Papamichael et al., 2012; Schroer et al., 2016). For instance, the short-wavelength light stronger suppresses melatonin production and distort circadian rhythms in mammals (Haim and Portnov, 2013; Hatori et al., 2017; Lockley et al., 2003), while the long-

wavelength light stronger disrupts the magnetic orientation of migratory birds (Wiltschko et al., 1993). As far as adverse effects of NTL become more recognized to depend on light spectrum, multispectral satellite imagery analysis becomes more numerous (Guk and Levin, 2020; Huang et al., 2021; Levin and Duke, 2012; Rybnikova and Portnov, 2017; Zheng et al., 2018). Such studies usually aim at revealing associations between light of certain spectra and land-use types or economic activities. The assumption (either explicit or implicit) behind these studies is that different land use types or economic activities use predominantly certain lighting source type. In the meantime, direct discriminating between different lamp types based on satellite imagery would allow a more fine-tuned analysis of adverse health effects associated with NTL. In turn, this would contribute to elaborating more precise policies for diminishing light pollution.

Such studies, aiming to directly link NTL spectra with onground lamp types, remain, however, extremely limited (Elvidge et al., 2010; Hale et al., 2013; Sánchez de Miguel et al., 2019; Zheng et al., 2018). In two of them (Elvidge et al., 2010; Sánchez de Miguel et al., 2019), the authors tested the principal possibility to identify lamp type, proceeding from corresponding spectral signature, either detailed or aggregated. In the first study, Elvidge with co-authors analysed spectral signatures of 43 different lamps representing nine the most widespread lamp types, using ASD spectroradiometer, implying measuring the signatures from 400 to 2500 nm with 10 nm band width (Elvidge et al., 2010). They showed that discriminant analysis correctly classified all lamp types when based on their detailed spectra. The authors also succeeded to find a minimum set of broad bands ensuring sufficient classification quality: Under blue, green, red, and NIR bands (a slightly modified set represented on the Landsat Thematic Mapper), only 4.7% of the lamp types were classified incorrectly. In the second study by de Miguel with co-authors, it was demonstrated that main lamp types can often be separated using color-color diagrams with G/R and B/G ratios

as the two coordinates (Sánchez de Miguel et al., 2019). At that, the RGB bands corresponded to Nikon D3s camera sensors, used by astronauts in the ISS. However, in both mentioned studies, the proposed lamp-type discriminating methods, although being based on spectral bands of existing satellites, were not tested on real imagery (Elvidge et al., 2010; Sánchez de Miguel et al., 2019).

To the best of our knowledge, the only explicit tests of such kind were performed in (Hale et al., 2013; Zheng et al., 2018). Thus, Hale with co-authors analysed a one-meter aerial image of the Birmingham city, UK, and a layer reporting location and type of lamp (Hale et al., 2013). They succeeded to classify four main lamp types with high accuracy (7.5% error), based on three focal statistics: B and G/R ratio for pixels up to 1 m from the lamp centre and the maximum averaged RGB level for pixels between 2 and 4 m from the lamp centre. At that, RGB bands corresponded to those of Nikon D2X digital camera. Zheng with co-authors, in the meantime, used RGB high-resolution (0.92 m) commercial satellite JL1-3B image to discriminate between HPS and LED lamps – two most widespread lighting sources in the study area, represented by Hangzhou, China (Zheng et al., 2018). The authors used RGB levels of brightly lit pixels of the image as input data for ISODATA clustering procedure; While unlabelled classes, generated by clustering algorithm, together with morphological characteristics of bright pixels, were used as inputs in decision tree classification procedure to discriminate HPS from LED lamps. The authors matched each group of bright pixels in the satellite image with lighting source type, obtained from the field survey and report that upon 446 available observations, overall accuracy of classification reaches 83.86%. These studies, however, benefit from high-resolution aerial images available only for limited sites and are typically costly.

In the present study, we test for the possibility to identify on-ground lamp types from freely available satellite imagery of relatively coarse spatial and spectral resolution. For the study area of

Haifa, Israel, we superimpose two NTL data sources: (*i*) the radiometrically calibrated broadband RGB image provided by the ISS, and (*ii*) a set of *in situ* measurements with detailed spectral signatures conducted by ourselves. Since the ISS image is of ~20-meter resolution, each pixel likely represents a *mixture of lamps*. Thus, the detailed spectral signatures of the *in situ* measurements are first subjected to unmixing analysis, with the standard lamp types used as endmembers, – to estimate the relative contribution of different lamp types in each measurement. Afterward, we use the levels of RGB bands of the corresponding pixels in the ISS image and develop statistical models to predict the relative contribution of different lamp type (output) from the aggregated RGB data (input). Finally, we apply the successful models to all pixels from the ISS image to restore the maps of relative contribution of certain lamp types into outdoor lighting in Haifa area.

2. Data Sources

The ISS-produced NTL image of Haifa (ISS045-E-148262) was taken on November 29, 2015 with the Nikon D4 DSLR camera ("Search Photos," n.d.). The image was georeferenced and radiometrically calibrated by SAVESTARS Consulting SL ("Home - Savestars Consulting S.L.," n.d.) according to the procedure reported in (Sánchez de Miguel, 2021). *In situ* NTL measurements were performed in March 2015 with the Konica Minolta CL-500A spectrometer. Each of the 610 measurements reports spectral irradiance (w/m^2) at 1-nm pitch from 360 to 780 nm ("Illuminance Spectrophotometer CL-500A," n.d.). Fig. 1 reports the original and the radiometrically calibrated RGB images from the ISS, overlaid with the *in situ* measurements localities.

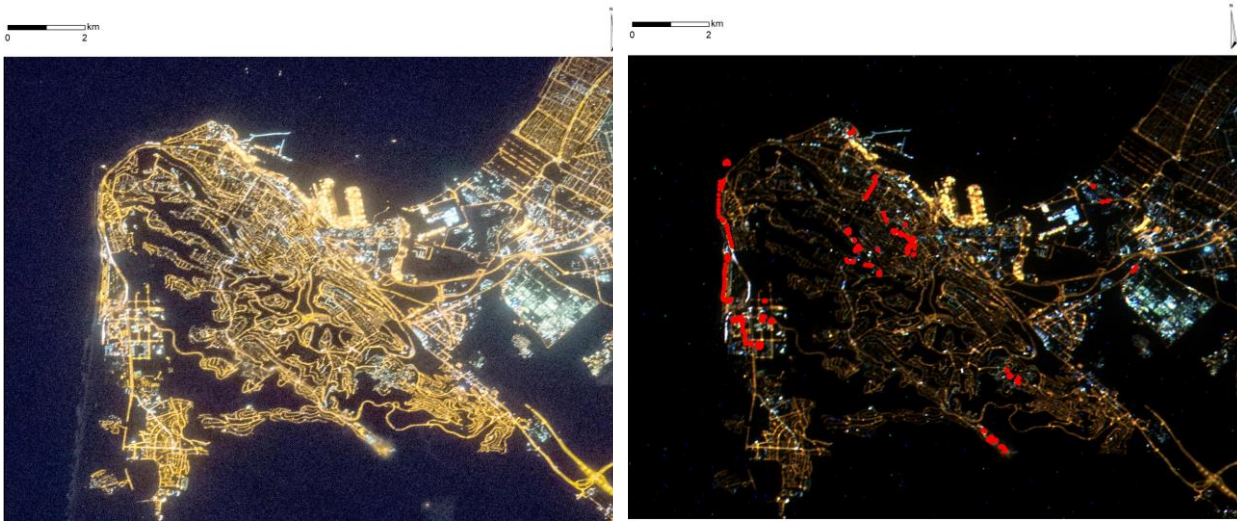

(a) *(b)*

Figure 1: Georeferenced ISS-produced (taken on 29.11.2015 by Nikon D4 DSLR camera; ID ISS045-E-148262) *(a)* and radiometrically calibrated *(b)* night-time image of the Haifa region. *In situ* measurements (n=610), performed in March 2015 *via* Konica Minolta CL-500A spectrometer, are marked by red dots in the left sub-figure.

The spectral signatures of standard lamp types were taken from the LICA UCM library (Tapia Ayuga et al., 2017). We examined spectral signatures of 81 lamps representing seven (out of nine reported by Elvidge et al. (2010)) the most popular lamp types: fluorescent (FL), metal-halide (MH), high-pressure sodium (HPS), low-pressure sodium (LPS), incandescent and halogen (I&H), mercury-vapor (MV), and light-emitting diodes (LED). Two other widespread lighting types, liquid-fuel and pressurized-fuel lamps, were omitted due to the data unavailability.

3. Methods

The methodological scheme of the study is reported in Fig. 2 and described in detail in subsections below.

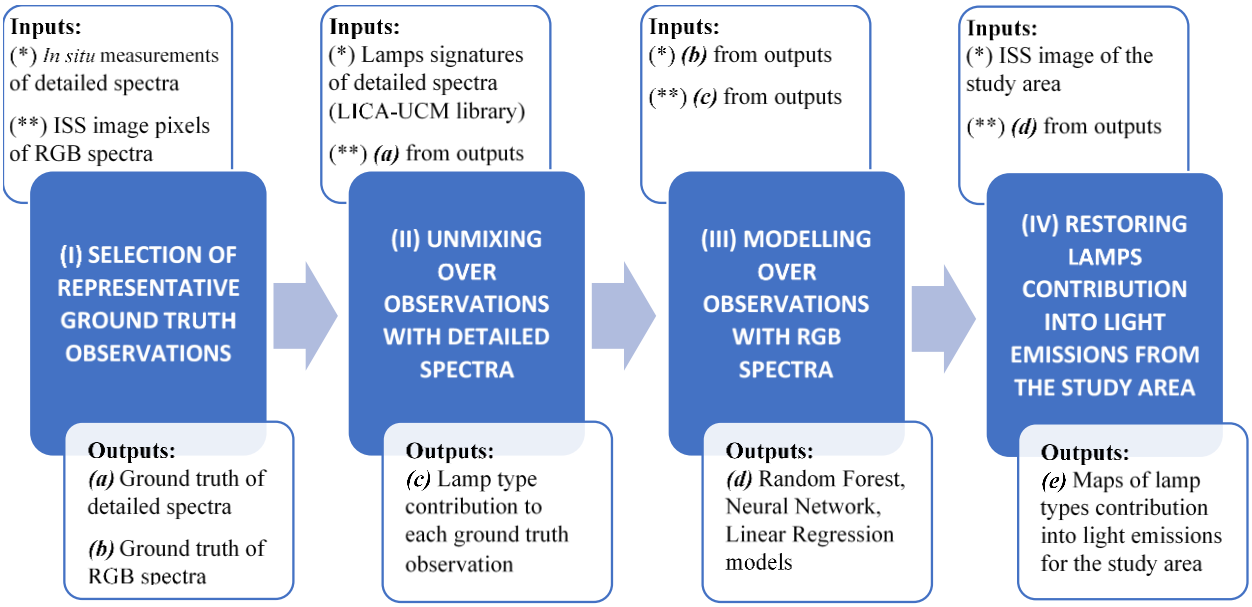

Figure 2: Methodological scheme of the study

3.1 Selection of the representative in situ measurements for the ground truth

Proceeding from the available data on relatively coarse spatial resolution of ISS image, with each pixel reporting emissions from multiple light sources, and simultaneously given the sporadic point-wise available *in situ* NTL measurements, we selected among 610 observations only those which *in some sense* coincided with corresponding pixels in the ISS image. Since each pixel might be characterized by RGB radiances only, we first simulated the radiances of synthetic RGB bands of *in situ* measurements as if they would appear on the ISS sensors of Nikon D4 DSLR camera, and then chose the observations with similar (to the corresponding ISS imagery pixel) RGB characteristics.

To simulate the radiance R (of either red, green, or blue band), we used the augmented equation reported by Sanchez de Miguel et al. (2019):

$$R = \frac{\int_0^\infty \phi(\lambda)T(\lambda)A(\lambda)d\lambda}{\int_0^\infty \phi_{AB}(\lambda)T(\lambda)A(\lambda)d\lambda}, \qquad (1)$$

where

$\phi(\lambda)$ = spectrum of the lamp under analysis;

$T(\lambda)$ = spectral sensitivity of the synthetic band (in the present analysis, we used spectral responses of Nikon D4 Electronic Still Camera – the one produced the image under analysis, – reported in (Sánchez de Miguel et al., 2019)) – see Fig. 3*(a)*;

$A(\lambda)$ = atmospheric transmittance (in the present analysis, we applied the MODTRAN® computer code ("MODTRAN®," n.d.) for the simulation of atmospheric transmittance of light emissions through the atmosphere over the study area at the time when *in situ* measurements were performed) – see Fig. 3*(b)*;

$\phi_{AB}(\lambda)$ = reference spectrum of AB magnitude system, defined for a source of constant spectral density flux of 3631 Janskys across the spectral range of the band (Sánchez de Miguel et al., 2019) – see Fig. 3*(c)*.

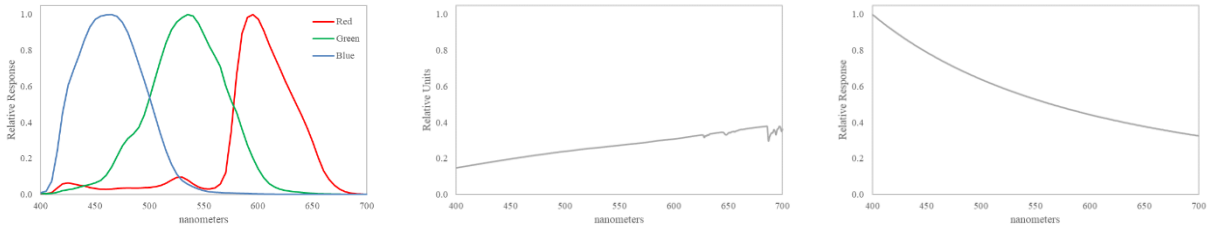

(a) *(b)* *(c)*

Figure 3: Graphical illustration of the constituents for synthetic bands' radiance computation: Spectral sensitivity of RGB bands of Nikon D4 DSLR camera *(a)*, Atmospheric transmittance *(b)*, and Reference spectrum of AB magnitude system *(c)*.

As a measure of similarity between RGB radiances, reported by pixels of calibrated ISS image, and corresponding *in situ* measurements, we used Euclidian distance in the coordinate system, represented by B/G and G/R ratios. Given the variance of such a distance (d_{max} = 2.00), we settled the threshold of d<0.2.

3.2 Unmixing of the detailed spectral signatures of the representative in situ measurements

The detailed spectral signatures of the representative *in situ* measurements (see subsection 3.1) were subjected to unmixing analysis. As the endmembers (i.e., spectra of pure 'materials' – see (Shi and Wang, 2014)), we used the detailed spectral signatures of the standard lamps from LICA-UCM library. The endmembers' signatures are shown in Fig. 4. For unmixing analysis, we used the FNNLS algorithm (Bro and De Jong, 1997), implemented in MATLAB v.R2020b. The algorithm returned the percentages of all endmember lamps in each of the pre-selected *in situ* measurements. The obtained percentages were then aggregated within lamp types, and the sums were normalized to unit.

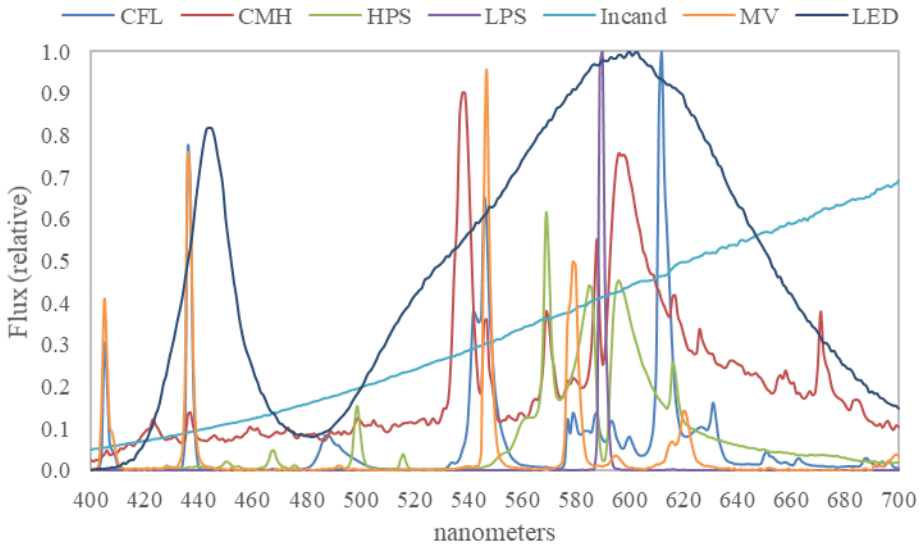

Figure 4: Spectral signatures of representatives of each lamp type used in the analysis.

Note: The following lamps' signatures are depicted: 'CFL' = Compact Fluorescent Lamp of 2776K; 'CMH' = Ceramic Metal Halide of 2829K; 'HPS' = High Pressure Sodium of 2005K; 'LPS' = Low Pressure Sodium of 1701K; 'Incand' = Incandescent Tungsten of 2805K; 'MV' = Mercury Vapor of 4717K; 'LED' = LED of 3033K.

3.3 Statistical Models to predict the relative contribution of different lamp types from the ISS image

The percentage of each lamp type, obtained in the unmixing analysis (Subsection 3.2), served as the dependent variable in a set of statistical models. As the explanatory variables, we tried different characteristics of the pixels of the calibrated ISS image: (*i*) radiance in the red, green and blue bands *per se*; (*ii*) their ratios (G/R and B/G, or GG/RB ratio), and an additional derivative characteristic describing the pixel's 'proximity' to the lamp type in question. This distance was included in the models since we found that different lamps within each of the lamp type tend to lie along straight lines in the G/R, B/G coordinate plane (see Fig. 5). We tried several formalizations of such a distance: (*i*) the ratio between B/G and G/R of the pixel, as a measure of the line's slope; (*ii*) Euclidean distance from the pixel to the line representing the lamp type in question, and (*iii*) Mahalanobis distance from the pixel to the cloud representing the lamp type in question, which accounts for both the centre of mass and the direction of the cloud (Mahalanobis, 1936).

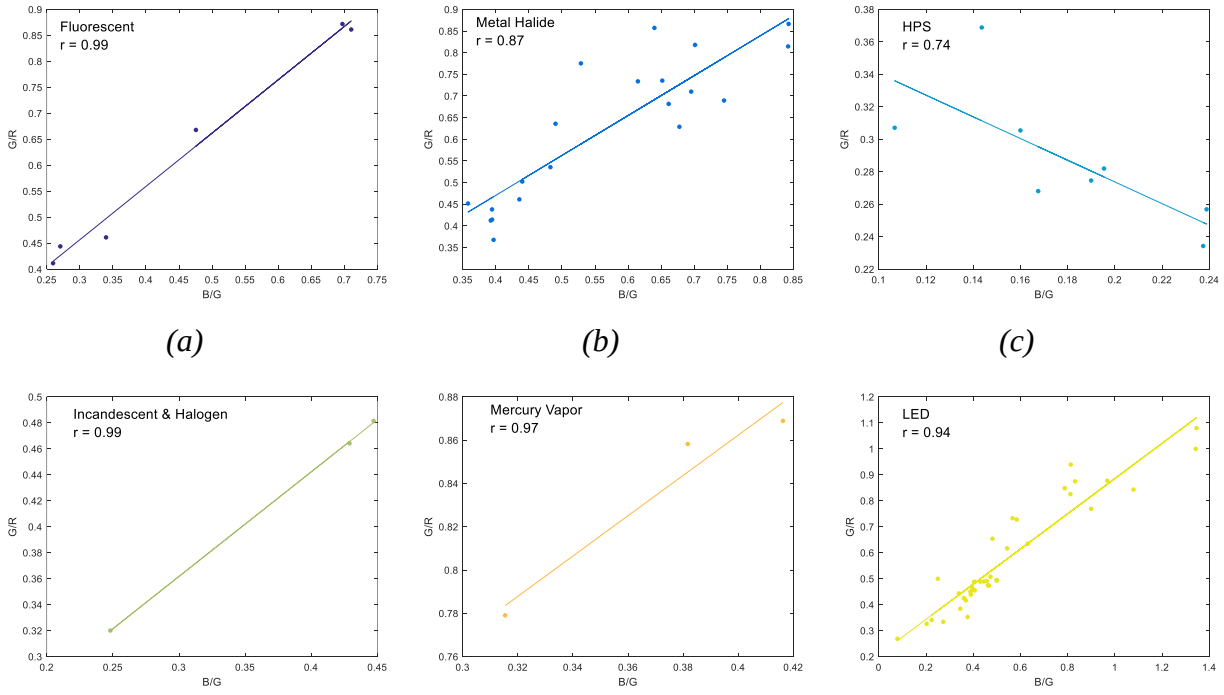

(a) *(b)* *(c)*

(d) *(e)* *(f)*

Figure 5: Simulated synthetic bands of the lamps: B/G *vs*. G/R ratios.

Note: LPS lamp, reporting G/R=0.18 and B/G=0.02, is the only representative of the type, and is not depicted in the figure

We examined statistical models of several classes: linear regression, neural network, and random forest. All models were run in ORANGE v.3.28 with the default settings. Specifically, *linear regression* was applied with intercept and without regularization. As a *neural network*, we used a multi-layer perceptron with backpropagation; the model parameters were the following: number of neurons in hidden layer is 100, number of hidden layers is 1, activation function is ReLu, solver for weight optimization is stochastic gradient-based optimizer, L2 penalty parameter is 0.0001, maximal number of iterations is 200. In *random forest* models, the number of trees was settled to 10, arbitrary set of attributes and limit depth of individual trees were left unchecked, and subsets smaller than 5 were required not to be split. The whole set of observations was split into the training (90%) and the testing (10%) subsets; the models were run ten times, and the average values were assigned to each model as its performance score. The input database used in the analysis is available from the authors upon request.

3.4 Restoring the relative contributions of different lamp types into light emissions in Haifa

Finally, the best-performing models (Subsection 3.3) were applied to the radiometrically calibrated ISS image (see Subsection 3.1), and estimates for different lamps' contribution into light emissions from the study area were obtained and depicted.

4. Results

Among all initially available *in situ* measurements, we chose the set of *representative* measurements – those deviating from the corresponding pixels of the radiometrically calibrated ISS image by less than 0.2 in terms of the Euclidian distance in the G/R, B/G coordinate plane (see

Subsection 3.1). Overall, we obtained 196 measurements; their main characteristics are reported in Fig. 6.

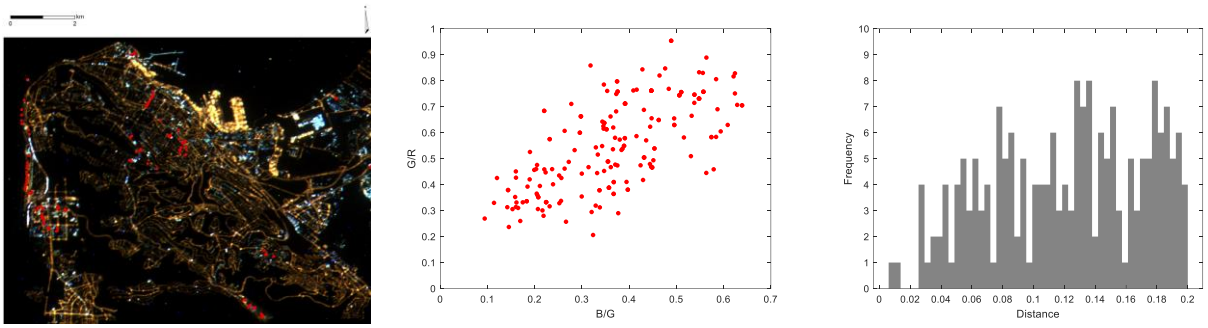

(a) *(b)* *(c)*

Figure 6: Main characteristics of selected representative ground truth measurements: Localities (marked as red dots) *(a)*, G/R & B/G ratios *(b)*, and Euclidian distances distribution from the corresponding ISS pixel in G/R, B/G coordinate system *(c)*

The detailed spectral signatures of the obtained 196 representative *in situ* measurements were then subjected to *unmixing analysis* (see subsection 3.2). The results of the unmixing, i.e. the percentages of the seven endmember lamp types, are reported in the Supplementary Table S1. In the table we also report, for each *in situ* measurement, the highest correlation between its detailed spectral signature and the signatures of the lamps from the LICA-UCM library. As one can see from the table, the measurements with predominant percentage of a certain lamp type (marked grey) simultaneously demonstrated high correlation with this lamp type. Overall, HPS lamps were the most widespread in Haifa in 2015 (average percentage 32.8%), followed by MH lamps (22.0%), while LED lamps were considerably less frequent (15.6%).

Table 1 reports the performance of three alternative statistical models (linear regression, neural network, and random forest) developed to explain the variance of each lamp type percentage, under various sets of predictors, for the training and the testing sets (see Subsection 3.3). As can it be seen from the table, the performance is higher for the models with G/R and B/G ratios as predictors, compared to those with R, G and B bands *per se*. For all dependent variables and all predictor sets,

random forest models perform better than either linear regression or neural network models. For three lamp types (HPS, MH, and MV), random forest models containing G/R and B/G ratios as predictors demonstrate high performance both for the training and the testing sets: R^2>0.782 (Table 1, predictor sets 2nd-4th).

Table 1: The performance of models (in terms of R^2) with alternative predictor sets, for the training and the testing sets (Dependent variable = Percentage of a certain lamp type)

Model Type	Subset	Lamp Type						
		HPS	MH	LED	CFL	LPS	Incand	MV
Predictor set 1: R, G, B								
Linear regression	Training	0.330	0.238	0.021	0.056	0.161	0.079	0.172
	Testing	0.454	0.140	0.004	0.041	0.125	0.149	0.158
Neural network	Training	0.387	0.043	-0.435	-0.296	-0.920	-0.298	-0.679
	Testing	0.354	0.341	-0.363	-0.449	-1.193	-0.664	-0.177
Random forest	Training	0.887	0.842	0.751	0.773	0.839	0.835	0.832
	Testing	0.442	0.819	0.510	0.523	0.340	0.089	0.701
Predictor set 2: G/R, B/G, GG/RB								
Linear regression	Training	0.516	0.328	0.020	0.116	0.236	0.082	0.227
	Testing	0.591	0.379	-0.022	-0.032	-0.172	0.123	0.158
Neural network	Training	0.524	0.368	0.040	0.137	0.208	0.160	0.300
	Testing	0.528	0.486	-0.161	-0.007	-0.274	0.140	0.167
Random forest	Training	0.872	0.847	0.641	0.791	0.831	0.712	0.870
	Testing	0.848	0.813	0.792	0.461	0.493	0.162	0.900
Predictor set 3: G/R, B/G, Mahalanobis distance								
Linear regression	Training	0.521	0.345	0.026	0.116	0.234	0.098	0.356
	Testing	0.580	0.374	-0.043	-0.026	-0.140	0.166	0.233
Neural network	Training	0.241	0.392	0.056	0.132	0.155	0.124	0.262
	Testing	0.271	0.482	-0.354	-0.229	-0.196	0.061	0.254
Random forest	Training	0.882	0.826	0.767	0.734	0.815	0.792	0.839
	Testing	0.811	0.806	0.373	0.616	0.492	0.675	0.786
Predictor set 4: G/R, B/G, Euclidean distance to the line								

Linear regression	Training	0.516	0.329	0.048	0.115	0.234	0.103	0.305
	Testing	0.593	0.383	-0.046	-0.023	-0.140	0.124	0.156
Neural network	Training	0.251	0.335	0.092	0.109	0.155	0.128	0.283
	Testing	0.225	0.495	-0.266	-0.307	-0.196	0.173	0.299
Random forest	Training	0.860	0.826	0.745	0.778	0.815	0.795	0.857
	Testing	0.815	0.782	0.286	0.577	0.492	0.675	0.838

Note: The lamps are sorted from left to right in descending order of their relative percentages (see results of unmixing analysis, reported in Table S1).

Since models with the predictor sets 2nd-4th demonstrate similar performance, and proceeding from consideration of calculation simplicity, we run random forest models with G/R, B/G, and GG/RB ratios as predictors upon all pixels of the calibrated ISS image (see Fig.1*(b)*). Fig. 7 reports resulting maps for two the most frequent lamp types' (HPS and MH) prevalence in Haifa. As can be seen from the figure, relatively higher contribution of HPS lamps in the outdoor lighting in Haifa coincide with the spatial pattern of municipal roads (see Fig. 7 *(a)*), while the pattern for MH lamps is more local and site-specific (see Fig. 7 *(b)*). In some regions of interest, HPS and MH lamps contribute to the outdoor lighting reversely. For example, in the Haifa Bay area, the impact of HPS lamps is pronounced while MH lamps are absent (see Figs. 7 *(c)*); in contrast, in the areas hosting Khof Shemen industrial zone and Haifa airport, MH lamps are widely used while HPS lamps are absent (see Fig. 7 *(d)*).

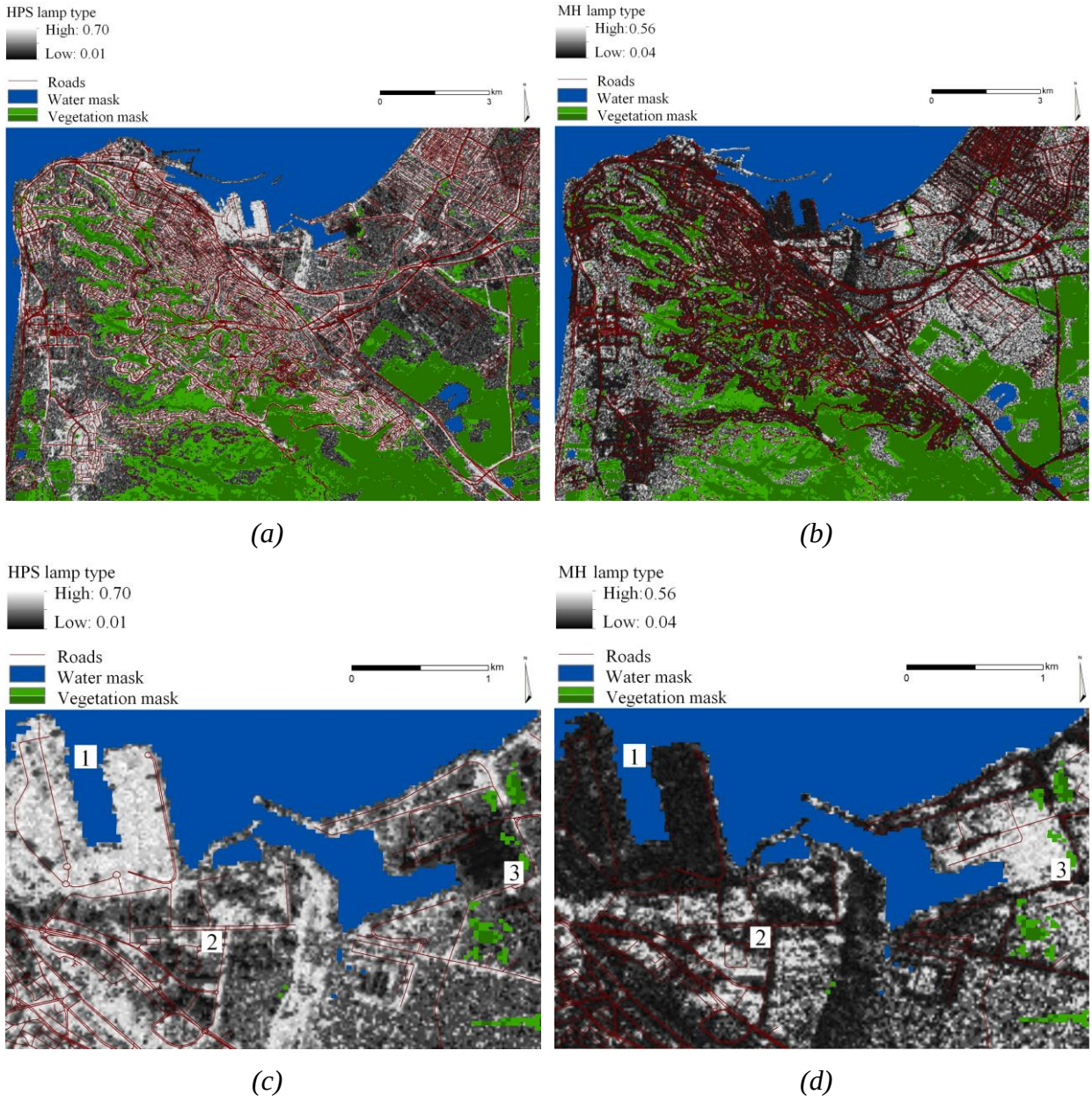

Figure 7: Model-anticipated relative contribution of High Pressure Sodium *((a)&(c))* and Metal Halide *((b)&(d))* lamps in the outdoor lighting in Haifa area *((a)&(b))* and selected ROIs *((c)&(d)):* "1" = Haifa Bay Area; "2" = Khof Shemen Industrial Zone; "3" = Haifa Airport.

Note: Water and vegetation masks (marked respectively blue and green) were produced from Landsat 8 OLI/TIRS C2 L2 dataset image (path 174 row 037) acquired on June 8, 2015 ("EarthExplorer," n.d.). For vegetation mask, normalized difference vegetation index (NDVI) was calculated as NDVI = (Band5 – Band6)/(Band5 + Band6) ("Landsat Normalized Difference Vegetation Index," n.d.), and levels in 0.22-0.25 and >0.25 diapasons were marked as light and dark green. For water mask, normalized difference moisture index (NDMI) was calculated as NDMI = (Band5 – Band4)/(Band5 + Band4) ("Normalized Difference Moisture Index," n.d.), and levels exceeding … were marked blue.

5. Discussion

In the present study, we tested for the possibility to identify on-ground lamp types from freely available satellite imagery of relatively coarse spatial and spectral resolution. To this end, we conducted a series of *in situ* NTL measurements in Haifa, Israel, and combined these data with a radiometrically calibrated NTL image of the city taken from the ISS. Since the ISS image is of ~20-meter resolution, each pixel likely represents light emission from a mixture of lamps. By applying unmixing analysis to the detailed spectral signatures, we estimated the relative contributions of different lamp types in the *in situ* measurements. Then, we tried to train statistical models to predict these contributions based exclusively on the ISS image, which represents broad spectral RGB bands.

As our analysis indicates, contributions of two the most widespread lamp types in the region, HPS and MH lamps, could be successfully predicted (with adjusted R^2 reaching 0.882 for the training and 0.848 for the testing sets) by random forest models. Using them, we restored HPS and MH lamps' contribution into outdoor lighting in all Haifa area. The obtained HPS map demonstrated high concordance with the network of municipal roads, while MH map showed notable coincidence with industrial facilities and airport (see Fig. 7).

In the developed models, we used three explanatory variables. Two of them, G/R and B/G ratios, are similar to those previously used by Sánchez de Miguel (2019). An additional informative predictor described a 'proximity' of the analysed pixel of the ISS image to the lamp type in question. Interestingly, it turned out that lamps of the same type form clear-cut line segment-shaped loci in the G/R, B/G coordinate plane (see Fig. 5). With this respect, we tried three alternative formalizations for the above-mentioned proximity: GG/RB ratio of the pixel, its Euclidean distance to the line, and, and its Mahalanobis distance to the locus. Without this

additional explanatory variable, the models' performance was somewhat worse (with adjusted R^2<0.861 for the training and R^2<0.828 for the testing sets).

It should be mentioned that both Elvidge *et al*. (2010), Hale *et al.* (2013), and Zheng *et al.* (2018) reached remarkably high classification accuracy (with errors 4.7%, 7.5%, and 16.1% respectively). However, their results cannot be directly compared with those presented here since we solved regression rather than classification problem, implying continuous rather that binary dependent variable. Yet, it seems reasonable to expect better performance of our models if they were based on an image of better spectral (like in (Elvidge et al., 2010)) and/or spatial (like in (Hale et al., 2013; Zheng et al., 2018)) resolution. Again, as mentioned above, we used the ISS image intentionally – given its free availability for many geographical sites. We think that our results argue for the principal possibility to assess the lamp type composition of outdoor lighting from the color satellite imagery.

Some limitations and perspectives of the study should be mentioned. First, proceeding from the available data, we did not succeed to obtain a reasonable spatial pattern for LEDs' contribution in the outdoor lighting in Haifa. A trivial reason may be insufficiency of the used data (small sample size, low prevalence of LEDs in the studied region in 2015). It also seems possible that the ISS imagery does not allow discriminating LEDs due to their high spectral variability and, therefore, overlapping with some other lamp types (which becomes even more pronounced after considering the reflectance of the ground), such as MH lamps, in the B/G, G/R space (Sánchez de Miguel et al., 2019). It should be mentioned that Elvidge et al. (2010) did succeed to discriminate LED lamps from other types since they used almost non-overlapping red, green, blue, and NIR bands. Nowadays, LEDs' popularity grows rapidly (Alamús et al., 2017; Elvidge et al., 2010; Sánchez de Miguel et al., 2019; Schubert and Kim, 2005) mainly due to their versatility and energy saving

potential, and some precedents of total LED-based street lighting already exist (Kyba et al., 2020; Sánchez de Miguel et al., 2019). At the same time, LEDs' primary emission peak, ~450-460 nm (Elvidge et al., 2010), extremely distorts circadian rhythms and suppresses melatonin production in humans, contributing to sleep disorders (Czeisler, 2013), obesity (McFadden et al., 2014), hormone-dependent cancers (Haim and Portnov, 2013), and other diseases. Thus, further analysis is needed to explore the possibility to identify LED lamps from the ISS-provided imagery. It seems promising to exploit, in addition to ISS imagery, VIIRS-provided data, which covers also NIR diapason on night-time light.

Second, acquisition time of the used ISS-provided image and of the *in situ* NTL measurements do not coincide perfectly, which may cause some inaccuracy in the herein obtained estimates. However, weather conditions in Israel are rather similar in March (when the *in situ* measurements were conducted) and in November (when the ISS image was taken). Additionally, our sample did not include observations from residential areas, which brightness may vary during the night (Bará et al., 2019); instead, it included observations along major roads, entertainment areas, hospitals, and high-tech enterprises – that is, represented by streetlights of nearly-constant brightness during the night.

6. Conclusions

Numerous medical and environmental studies have shown that night-time light of different spectra differs in its impact on human and ecosystem health. With this respect, the development of smart and precise policies for diminishing the adverse effects of light pollution requires fine-tuned analysis of multispectral satellite imagery which would enable remote recognition of different on-ground light sources. In the present study, we introduce a new approach to discriminate between lamp types proceeding from the freely available night-time ISS imagery and test it over the Haifa

region, Israel. At the first stage, we applied unmixing analysis to the detailed spectral signatures of in situ measurements – to characterize each measurement by a set of percentages estimating the relative contributions of different lamp types to the overall light emission. Afterward, we matched the in situ measurements with the corresponding pixels in the ISS image and used the RGB characteristics (that is, G/R, B/G ratios, and the ratio between the two) of these pixels as explanatory variables in a set of machine learning techniques – to predict the earlier obtained percentages of different lamp types. For two lamp types, HPS and MH lamps, the predictions appeared fairly accurate. The restored maps of the relative contribution of these lamp types demonstrated high spatial concordance with specific on-ground activities, such as the network of municipal roads (for HPS lamps) and industrial facilities and airport (for MH lamps). These two lighting sources are the most widespread in the study area. The third popular lighting source, LED lamps, appeared hard to predict. A possible way to discriminate LED lamps may be combining ISS imagery with VIIRS data since the latter cover also NIR diapason. Such a fusion is a promising direction for future investigations.

Funding:

This work was supported by the Council for Higher Education of Israel and Cities at Night Project.

References:

Alamús, R., Bará, S., Corbera, J., Escofet, J., Palà, V., Pipia, L., Tardà, A., 2017. Ground-based hyperspectral analysis of the urban nightscape. ISPRS J. Photogramm. Remote Sens. 124, 16–26. https://doi.org/10.1016/J.ISPRSJPRS.2016.12.004

Bará, S., Rodríguez-Arós, Pérez, M., Tosar, B., Lima, R.C., Sánchez de Miguel, A., Zamorano, J., 2019. Estimating the relative contribution of streetlights, vehicles, and residential lighting to the urban night sky brightness. Light. Res. Technol. 51, 1092–1107. https://doi.org/10.1177/1477153518808337

Brainard, G.C., Hanifin, J.R., Greeson, J.M., Byrne, B., Glickman, G., Gerner, E., Rollag, M.D., 2001. Action spectrum for melatonin regulation in humans: Evidence for a novel circadian photoreceptor. J. Neurosci. 21, 6405–6412. https://doi.org/10.1523/jneurosci.21-16-06405.2001

Bro, R., De Jong, S., 1997. A fast non-negativity-constrained least squares algorithm. J. Chemom. 11, 393–401. https://doi.org/10.1002/(SICI)1099-128X(199709/10)11:5<393::AID-CEM483>3.0.CO;2-L

Cho, S., Lee, M., Choi, H., Korean, H.K.-J. of the, 2011, undefined, 2011. Calculation and Regulation Proposal of Light Pollution from Road Lightings. koreascience.or.kr 21–26. https://doi.org/10.5207/JIEIE.2011.25.12.021

Cinzano, P., Falchi, F., Elvidge, C.D., 2001. The first World Atlas of the artificial night sky brightness. Mon. Not. R. Astron. Soc. 328, 689–707. https://doi.org/10.1046/j.1365-8711.2001.04882.x

Czeisler, C.A., 2013. Perspective: Casting light on sleep deficiency. Nature 497, S13. https://doi.org/10.1038/497S13a

EarthExplorer [WWW Document], n.d. URL https://earthexplorer.usgs.gov/ (accessed 6.22.21).

Elvidge, C.D., Keith, D.M., Tuttle, B.T., Baugh, K.E., 2010. Spectral identification of lighting type and character. Sensors 10, 3961–3988. https://doi.org/10.3390/s100403961

Falchi, F., Bará, S., 2020. A linear systems approach to protect the night sky: implications for current and future regulations. R. Soc. Open Sci. 7. https://doi.org/10.1098/RSOS.201501

Falchi, F., Cinzano, P., Duriscoe, D., Kyba, C.C.M., Elvidge, C.D., Baugh, K., Portnov, B.A., Rybnikova, N.A., Furgoni, R., 2016. The new world atlas of artificial night sky brightness. Sci. Adv. 2, e1600377. https://doi.org/10.1126/sciadv.1600377

Garcia-Saenz, A., Sánchez de Miguel, A., Espinosa, A., Valentin, A., Aragonés, N., Llorca, J., Amiano, P., Martín Sánchez, V., Guevara, M., Capelo, R., Tardón, A., Peiró-Perez, R., Jiménez-Moleón, J.J., Roca-Barceló, A., Pérez-Gómez, B., Dierssen-Sotos, T., Fernández-Villa, T., Moreno-Iribas, C., Moreno, V., García-Pérez, J., Castaño-Vinyals, G., Pollán, M., Aubé, M., Kogevinas, M., 2018. Evaluating the Association between Artificial Light-at-Night Exposure and Breast and Prostate Cancer Risk in Spain (MCC-Spain Study). Environ. Health Perspect. 126, 047011. https://doi.org/10.1289/EHP1837

Gaston, K., Duffy, J., Gaston, S., Bennie, J., Oecologia, T.D.-, 2014, U., 2014. Human alteration of natural light cycles: causes and ecological consequences. Oecologia.

Gaston, K.J., Bennie, J., Davies, T.W., Hopkins, J., 2013. The ecological impacts of nighttime light pollution: A mechanistic appraisal. Biol. Rev. 88, 912–927. https://doi.org/10.1111/brv.12036

Guk, E., Levin, N., 2020. Analyzing spatial variability in night-time lights using a high spatial resolution color Jilin-1 image – Jerusalem as a case study. ISPRS J. Photogramm. Remote Sens. 163, 121–136. https://doi.org/10.1016/j.isprsjprs.2020.02.016

Haim, A., Portnov, B.A., 2013. Light pollution as a new risk factor for human breast and prostate cancers, Light Pollution as a New Risk Factor for Human Breast and Prostate Cancers. Springer Netherlands. https://doi.org/10.1007/978-94-007-6220-6

Hale, J.D., Davies, G., Fairbrass, A.J., Matthews, T.J., Rogers, C.D.F., Sadler, J.P., 2013. Mapping Lightscapes: Spatial Patterning of Artificial Lighting in an Urban Landscape. PLoS One 8. https://doi.org/10.1371/journal.pone.0061460

Hatori, M., Gronfier, C., … R.V.G.A. and, 2017, U., 2017. Global rise of potential health hazards caused by blue light-induced circadian disruption in modern aging societies. nature.com.

Hölker, F., Wolter, C., Perkin, E.K., Tockner, K., 2010. Light pollution as a biodiversity threat. Trends Ecol. Evol. https://doi.org/10.1016/j.tree.2010.09.007

Home - Savestars Consulting S.L. [WWW Document], n.d. URL http://www.savestarsconsulting.com/en/index/ (accessed 5.6.21).

Huang, X., Yang, J., Li, J., Wen, D., 2021. Urban functional zone mapping by integrating high spatial resolution nighttime light and daytime multi-view imagery. ISPRS J. Photogramm. Remote Sens. 175, 403–415. https://doi.org/10.1016/J.ISPRSJPRS.2021.03.019

Illuminance Spectrophotometer CL-500A [WWW Document], n.d. URL https://www.konicaminolta.com/instruments/download/catalog/light/pdf/cl500a_catalog_eng.pdf (accessed 5.6.21).

Kloog, I., Haim, A., Stevens, R.G., Portnov, B.A., 2009. Global co-distribution of light at night (LAN) and cancers of prostate, colon, and lung in men. Chronobiol. Int. 26, 108–125.

Kyba, C.C.M., 2018. Is light pollution getting better or worse? Nat. Astron. https://doi.org/10.1038/s41550-018-0402-7

Kyba, C.C.M., Kuester, T., De Miguel, A.S., Baugh, K., Jechow, A., Hölker, F., Bennie, J., Elvidge, C.D., Gaston, K.J., Guanter, L., 2017. Artificially lit surface of Earth at night increasing in radiance and extent. Sci. Adv. 3, e1701528. https://doi.org/10.1126/sciadv.1701528

Kyba, C.C.M., Ruby, A., Kuechly, H.U., Kinzey, B., Miller, N., Sanders, J., Barentine, J., Kleinodt, R., Espey, B., 2020. Direct measurement of the contribution of street lighting to satellite observations of nighttime light emissions from urban areas. Light. Res. Technol. https://doi.org/10.1177/1477153520958463

Landsat Normalized Difference Vegetation Index [WWW Document], n.d. URL https://www.usgs.gov/core-science-systems/nli/landsat/landsat-normalized-difference-vegetation-index?qt-science_support_page_related_con=0#qt-science_support_page_related_con (accessed 6.22.21).

Levin, N., Duke, Y., 2012. High spatial resolution night-time light images for demographic and socio-economic studies. Remote Sens. Environ. 119, 1–10. https://doi.org/10.1016/j.rse.2011.12.005

Lockley, S., … G.B.-T.J. of clinical, 2003, U., 2003. High sensitivity of the human circadian melatonin rhythm to resetting by short wavelength light. J. Clin. Endocrinol. Metab. 88, 4502–4505.

Longcore, T., Environment, C.R.-F. in E. and the, 2004, U., 2004. Ecological light pollution. Wiley Online Libr.

Lyytimäki, J., 2015. Towards eco-efficient and enjoyable lighting. Br. GSDR.

Mahalanobis, P., 1936. On the generalized distance in statistics.

McFadden, E., Jones, M.E., Schoemaker, M.J., Ashworth, A., Swerdlow, A.J., 2014. The relationship between obesity and exposure to light at night: cross-sectional analyses of over 100,000 women in the Breakthrough Generations Study. Am. J. Epidemiol. 180, 245–250.

MODTRAN® [WWW Document], n.d. URL http://modtran.spectral.com/ (accessed 6.13.21).

Morgan-Taylor, M., 2015. Regulating light pollution in Europe: Legal challenges and ways forward.

Normalized Difference Moisture Index [WWW Document], n.d. URL https://www.usgs.gov/core-science-systems/nli/landsat/normalized-difference-moisture-index (accessed 6.22.21).

Owens, A.C.S., Cochard, P., Durrant, J., Farnworth, B., Perkin, E.K., Seymoure, B., 2020. Light pollution is a driver of insect declines. Biol. Conserv. 241, 108259. https://doi.org/10.1016/j.biocon.2019.108259

Papamichael, C., Skene, D.J., Revell, V.L., 2012. Human Nonvisual Responses to Simultaneous Presentation of Blue and Red Monochromatic Light: http://dx.doi.org/10.1177/0748730411431447 27, 70–78. https://doi.org/10.1177/0748730411431447

Riegel, K.W., 1973. Light pollution. Science (80-.). 179, 1285–1291. https://doi.org/10.1126/science.179.4080.1285

Rybnikova, N.A., Portnov, B.A., 2017. Remote identification of research and educational activities using spectral properties of nighttime light. ISPRS J. Photogramm. Remote Sens. 128, 212–222. https://doi.org/10.1016/j.isprsjprs.2017.03.021

Sánchez de Miguel, A., 2021. Colour remote sensing of the impact of artificial light at night (II): Calibration of DSLR-based images from the International Space Station. Press.

Sánchez de Miguel, A., Kyba, C.C.M., Aubé, M., Zamorano, J., Cardiel, N., Tapia, C., Bennie, J., Gaston, K.J., 2019. Colour remote sensing of the impact of artificial light at night (I): The potential of the International Space Station and other DSLR-based platforms. Remote Sens. Environ. 224, 92–103. https://doi.org/10.1016/j.rse.2019.01.035

Schroer, S., Karlicek, F.H.-L.T., R., U., Sun, U., C.-C, U., 2016, U., 2016. Impact of Lighting on Flora and Fauna. researchgate.net. https://doi.org/10.1007/978-3-319-00295-8_42-1

Schubert, E.F., Kim, J.K., 2005. Solid-state light sources getting smart. Science (80-.). https://doi.org/10.1126/science.1108712

Search Photos [WWW Document], n.d. URL https://eol.jsc.nasa.gov/SearchPhotos/ (accessed 4.7.20).

Shi, C., Wang, L., 2014. Incorporating spatial information in spectral unmixing: A review. Remote Sens. Environ.

https://doi.org/10.1016/j.rse.2014.03.034

Tapia Ayuga, C., Sánchez de Miguel, A., Zamorano Calvo, J., 2017. LICA-UCM lamps spectral database. Ene 8, 29.

Wiltschko, W., Munro, U., Ford, H., Wiltschko, R., 1993. Red light disrupts magnetic orientation of migratory birds. Nature 364, 525–527. https://doi.org/10.1038/364525a0

Zhang, Q., Wang, P., Chen, H., Huang, Q., Jiang, H., Zhang, Z., Zhang, Y., Luo, X., Sun, S., 2017. A novel method for urban area extraction from VIIRS DNB and MODIS NDVI data: a case study of Chinese cities. Int. J. Remote Sens. 38, 6094–6109. https://doi.org/10.1080/01431161.2017.1339927

Zheng, Q., Weng, Q., Huang, L., Wang, K., Deng, J., Jiang, R., Ye, Z., Gan, M., 2018. A new source of multi-spectral high spatial resolution night-time light imagery—JL1-3B. Remote Sens. Environ. 215, 300–312. https://doi.org/10.1016/J.RSE.2018.06.016

Zheng, Q., Weng, Q., Wang, K., 2021. Characterizing urban land changes of 30 global megacities using nighttime light time series stacks. ISPRS J. Photogramm. Remote Sens. 173, 10–23. https://doi.org/10.1016/J.ISPRSJPRS.2021.01.002

SUPPLEMENTARY MATERIAL

Table S1: Unmixing results: The share of each lamp type in the detailed spectral signature of *in situ* observation (see text for explanation)

In situ obs. number	Share of lamp type in *in situ* observation detailed spectral signature (unmixing results)							Max correlation between detailed signatures of *in situ* obs. and lamps	
	CFL	MH	HPS	LPS	Incand	MV	LED	Correlation	Lamp type
504	0.085	0.659	0.067	0.060	0.014	0.000	0.114	0.720	LED
185	0.197	0.176	0.305	0.080	0.030	0.000	0.213	0.911	LED
566	0.022	0.058	0.201	0.044	0.568	0.009	0.097	0.957	Incand
467	0.000	0.024	0.772	0.054	0.000	0.000	0.150	0.945	HPS
238	0.194	0.072	0.323	0.000	0.008	0.307	0.095	0.634	MV
231	0.195	0.058	0.265	0.000	0.000	0.389	0.093	0.654	MV
97	0.000	0.065	0.664	0.169	0.000	0.000	0.101	0.937	HPS
465	0.000	0.024	0.760	0.103	0.000	0.000	0.113	0.930	HPS
286	0.083	0.465	0.336	0.000	0.000	0.000	0.116	0.747	LED
570	0.097	0.287	0.052	0.059	0.049	0.000	0.456	0.946	LED
112	0.040	0.305	0.372	0.243	0.013	0.000	0.026	0.806	HPS
565	0.000	0.019	0.151	0.027	0.638	0.002	0.164	0.979	Incand
431	0.000	0.056	0.671	0.151	0.036	0.000	0.087	0.889	HPS
466	0.000	0.024	0.755	0.100	0.000	0.000	0.121	0.932	HPS
433	0.000	0.085	0.629	0.119	0.000	0.000	0.166	0.913	LED
107	0.000	0.076	0.595	0.298	0.000	0.000	0.031	0.891	HPS
451	0.074	0.543	0.272	0.046	0.000	0.000	0.066	0.777	MH
1	0.247	0.098	0.161	0.000	0.000	0.386	0.108	0.670	MV
250	0.237	0.042	0.141	0.000	0.002	0.480	0.098	0.663	MV
432	0.000	0.068	0.608	0.075	0.062	0.000	0.187	0.936	LED
430	0.016	0.007	0.729	0.000	0.052	0.000	0.195	0.938	HPS
103	0.000	0.084	0.658	0.204	0.000	0.000	0.054	0.922	HPS
68	0.008	0.327	0.412	0.162	0.000	0.000	0.091	0.782	HPS
36	0.000	0.157	0.646	0.104	0.000	0.000	0.093	0.935	HPS
453	0.077	0.555	0.279	0.025	0.000	0.000	0.065	0.776	MH
168	0.025	0.358	0.478	0.045	0.000	0.000	0.094	0.849	HPS
40	0.000	0.058	0.674	0.176	0.000	0.000	0.092	0.935	HPS
64	0.021	0.345	0.411	0.148	0.000	0.000	0.074	0.741	HPS
440	0.007	0.184	0.584	0.107	0.000	0.000	0.118	0.898	HPS
452	0.078	0.551	0.269	0.041	0.000	0.000	0.062	0.775	MH
264	0.020	0.030	0.029	0.004	0.873	0.000	0.044	0.997	Incand
256	0.000	0.739	0.000	0.000	0.121	0.000	0.140	0.832	MH
261	0.392	0.152	0.235	0.045	0.026	0.000	0.149	0.843	LED
397	0.068	0.382	0.168	0.060	0.020	0.000	0.301	0.852	LED
109	0.000	0.081	0.586	0.311	0.000	0.000	0.023	0.885	HPS
445	0.036	0.511	0.294	0.116	0.008	0.000	0.035	0.803	MH

In situ obs. number	Share of lamp type in *in situ* observation detailed spectral signature (unmixing results)							Max correlation between detailed signatures of *in situ* obs. and lamps	
	CFL	MH	HPS	LPS	Incand	MV	LED	Correlation	Lamp type
38	0.020	0.092	0.604	0.134	0.000	0.000	0.150	0.928	LED
450	0.076	0.570	0.266	0.010	0.000	0.000	0.079	0.762	MH
528	0.124	0.154	0.384	0.068	0.000	0.155	0.116	0.725	LED
104	0.000	0.086	0.614	0.268	0.000	0.000	0.032	0.900	HPS
559	0.516	0.036	0.161	0.000	0.000	0.203	0.085	0.789	CFL
590	0.123	0.604	0.000	0.069	0.109	0.000	0.095	0.838	MH
29	0.114	0.090	0.525	0.094	0.002	0.000	0.174	0.930	LED
35	0.000	0.038	0.758	0.087	0.000	0.000	0.116	0.935	HPS
608	0.088	0.552	0.000	0.020	0.092	0.000	0.248	0.881	LED
187	0.004	0.123	0.574	0.151	0.008	0.000	0.140	0.927	HPS
31	0.055	0.060	0.640	0.152	0.000	0.000	0.093	0.926	HPS
129	0.000	0.052	0.693	0.181	0.000	0.000	0.074	0.931	HPS
508	0.409	0.409	0.044	0.000	0.000	0.025	0.112	0.714	CFL
260	0.034	0.675	0.149	0.086	0.000	0.000	0.057	0.752	MH
558	0.450	0.014	0.167	0.000	0.000	0.277	0.092	0.759	CFL
529	0.107	0.195	0.425	0.090	0.000	0.072	0.110	0.735	LED
556	0.532	0.038	0.153	0.000	0.000	0.198	0.079	0.797	CFL
564	0.000	0.045	0.239	0.060	0.455	0.000	0.202	0.934	Incand
518	0.013	0.027	0.103	0.045	0.049	0.000	0.762	0.983	LED
495	0.641	0.221	0.000	0.021	0.000	0.000	0.117	0.768	CFL
69	0.086	0.047	0.647	0.080	0.000	0.000	0.139	0.937	LED
429	0.000	0.045	0.688	0.000	0.070	0.000	0.197	0.930	HPS
101	0.000	0.071	0.643	0.179	0.000	0.000	0.106	0.934	HPS
291	0.093	0.263	0.296	0.000	0.005	0.155	0.189	0.725	LED
102	0.000	0.080	0.610	0.276	0.000	0.000	0.035	0.899	HPS
139	0.000	0.195	0.516	0.218	0.000	0.000	0.071	0.885	HPS
138	0.000	0.139	0.554	0.245	0.000	0.000	0.061	0.890	HPS
509	0.113	0.602	0.126	0.000	0.000	0.043	0.115	0.716	MH
100	0.000	0.086	0.547	0.367	0.000	0.000	0.000	0.841	HPS
607	0.053	0.554	0.000	0.000	0.111	0.000	0.282	0.887	LED
526	0.723	0.204	0.000	0.019	0.000	0.000	0.054	0.828	CFL
449	0.063	0.524	0.266	0.112	0.000	0.000	0.035	0.824	MH
517	0.038	0.184	0.492	0.219	0.000	0.000	0.067	0.840	HPS
520	0.002	0.000	0.004	0.000	0.057	0.018	0.919	0.984	LED
391	0.000	0.081	0.588	0.291	0.000	0.000	0.040	0.892	HPS
46	0.219	0.093	0.098	0.000	0.000	0.000	0.590	0.954	LED
523	0.016	0.133	0.439	0.373	0.000	0.000	0.040	0.766	HPS
519	0.028	0.002	0.009	0.000	0.060	0.021	0.880	0.984	LED
84	0.077	0.091	0.665	0.000	0.023	0.000	0.144	0.949	HPS
193	0.101	0.102	0.483	0.163	0.000	0.000	0.151	0.906	LED

In situ obs. number	Share of lamp type in *in situ* observation detailed spectral signature (unmixing results)							Max correlation between detailed signatures of *in situ* obs. and lamps	
	CFL	MH	HPS	LPS	Incand	MV	LED	Correlation	Lamp type
589	0.032	0.645	0.000	0.000	0.179	0.000	0.144	0.810	MH
524	0.032	0.127	0.365	0.252	0.000	0.000	0.225	0.858	LED
591	0.474	0.419	0.000	0.018	0.025	0.000	0.064	0.747	CFL
563	0.000	0.039	0.154	0.073	0.630	0.000	0.103	0.971	Incand
474	0.062	0.465	0.270	0.138	0.000	0.000	0.065	0.756	MH
16	0.028	0.013	0.189	0.021	0.028	0.019	0.701	0.977	LED
41	0.000	0.012	0.777	0.085	0.000	0.000	0.126	0.942	HPS
343	0.776	0.193	0.000	0.011	0.000	0.000	0.020	0.837	CFL
32	0.000	0.102	0.532	0.366	0.000	0.000	0.000	0.832	HPS
273	0.015	0.334	0.470	0.055	0.000	0.000	0.126	0.880	LED
208	0.005	0.108	0.344	0.150	0.032	0.000	0.361	0.965	LED
98	0.086	0.112	0.505	0.248	0.000	0.000	0.049	0.881	HPS
228	0.031	0.187	0.525	0.147	0.000	0.000	0.110	0.911	HPS
245	0.246	0.039	0.149	0.000	0.009	0.462	0.095	0.671	MV
446	0.023	0.537	0.293	0.126	0.000	0.000	0.021	0.820	MH
173	0.080	0.276	0.049	0.000	0.000	0.324	0.272	0.634	MH
605	0.082	0.548	0.000	0.017	0.091	0.000	0.262	0.893	LED
99	0.055	0.115	0.480	0.348	0.000	0.000	0.002	0.811	HPS
601	0.768	0.169	0.000	0.000	0.000	0.000	0.063	0.859	CFL
18	0.165	0.103	0.375	0.000	0.004	0.223	0.129	0.669	LED
555	0.609	0.069	0.123	0.000	0.000	0.126	0.073	0.818	CFL
530	0.473	0.079	0.080	0.030	0.000	0.062	0.275	0.772	LED
263	0.033	0.039	0.130	0.055	0.657	0.000	0.085	0.977	Incand
327	0.000	0.776	0.000	0.074	0.000	0.000	0.150	0.812	MH
600	0.767	0.165	0.000	0.000	0.000	0.000	0.068	0.856	CFL
557	0.305	0.015	0.191	0.000	0.000	0.403	0.087	0.678	MV
206	0.015	0.087	0.250	0.111	0.004	0.000	0.533	0.971	LED
562	0.000	0.058	0.201	0.106	0.527	0.000	0.108	0.936	Incand
265	0.024	0.015	0.038	0.013	0.895	0.002	0.012	0.999	Incand
372	0.093	0.076	0.160	0.039	0.525	0.000	0.106	0.957	Incand
604	0.032	0.525	0.000	0.000	0.115	0.000	0.328	0.916	LED
6	0.099	0.612	0.200	0.027	0.004	0.000	0.059	0.776	MH
606	0.047	0.558	0.000	0.000	0.114	0.000	0.282	0.885	LED
45	0.407	0.139	0.295	0.044	0.000	0.000	0.115	0.827	LED
266	0.052	0.031	0.032	0.010	0.843	0.000	0.032	0.998	Incand
39	0.000	0.052	0.673	0.179	0.000	0.000	0.096	0.935	HPS
15	0.019	0.014	0.089	0.013	0.037	0.022	0.805	0.976	LED
51	0.085	0.184	0.423	0.007	0.000	0.102	0.199	0.775	LED
583	0.094	0.573	0.217	0.000	0.000	0.000	0.115	0.729	MH
584	0.098	0.617	0.206	0.000	0.000	0.000	0.078	0.776	MH

In situ obs. number	Share of lamp type in *in situ* observation detailed spectral signature (unmixing results)							Max correlation between detailed signatures of *in situ* obs. and lamps	
	CFL	MH	HPS	LPS	Incand	MV	LED	Correlation	Lamp type
42	0.002	0.197	0.620	0.060	0.000	0.000	0.121	0.893	HPS
292	0.052	0.193	0.317	0.000	0.000	0.283	0.155	0.604	MV
461	0.037	0.596	0.105	0.162	0.000	0.000	0.100	0.826	MH
454	0.072	0.540	0.282	0.047	0.000	0.000	0.060	0.772	MH
439	0.011	0.081	0.619	0.146	0.001	0.000	0.141	0.917	HPS
471	0.057	0.469	0.271	0.141	0.000	0.000	0.062	0.772	MH
63	0.019	0.404	0.417	0.120	0.000	0.000	0.041	0.810	HPS
207	0.019	0.091	0.238	0.104	0.034	0.000	0.514	0.975	LED
468	0.000	0.031	0.743	0.091	0.000	0.000	0.136	0.933	HPS
585	0.151	0.436	0.187	0.000	0.000	0.078	0.148	0.652	CFL
599	0.757	0.165	0.000	0.000	0.000	0.000	0.078	0.853	CFL
197	0.114	0.138	0.415	0.210	0.000	0.000	0.123	0.887	LED
571	0.032	0.450	0.116	0.118	0.085	0.000	0.198	0.891	LED
434	0.000	0.080	0.687	0.131	0.000	0.000	0.101	0.928	HPS
448	0.063	0.501	0.275	0.128	0.000	0.000	0.034	0.807	MH
90	0.163	0.154	0.441	0.044	0.000	0.000	0.198	0.904	LED
399	0.060	0.308	0.158	0.060	0.116	0.006	0.292	0.899	LED
66	0.297	0.190	0.248	0.077	0.000	0.000	0.188	0.810	LED
375	0.043	0.249	0.466	0.100	0.000	0.000	0.142	0.926	LED
105	0.000	0.071	0.673	0.141	0.000	0.000	0.115	0.933	HPS
309	0.003	0.243	0.583	0.049	0.000	0.000	0.122	0.913	HPS
349	0.392	0.181	0.110	0.000	0.001	0.000	0.315	0.815	LED
198	0.010	0.119	0.535	0.310	0.000	0.000	0.026	0.867	HPS
475	0.055	0.488	0.255	0.142	0.000	0.000	0.060	0.780	MH
267	0.027	0.027	0.029	0.010	0.872	0.000	0.035	0.998	Incand
7	0.195	0.493	0.088	0.000	0.029	0.068	0.126	0.677	LED
227	0.006	0.128	0.606	0.159	0.000	0.000	0.101	0.919	HPS
199	0.003	0.111	0.549	0.312	0.000	0.000	0.025	0.871	HPS
262	0.679	0.175	0.021	0.029	0.000	0.000	0.096	0.791	CFL
244	0.239	0.042	0.147	0.000	0.048	0.432	0.093	0.672	MV
189	0.099	0.041	0.627	0.042	0.000	0.000	0.191	0.922	LED
5	0.041	0.569	0.274	0.084	0.000	0.000	0.032	0.817	MH
52	0.125	0.229	0.276	0.055	0.000	0.099	0.217	0.832	LED
376	0.060	0.251	0.449	0.097	0.000	0.000	0.142	0.930	LED
545	0.024	0.139	0.523	0.297	0.000	0.000	0.018	0.829	HPS
527	0.170	0.167	0.400	0.132	0.000	0.000	0.131	0.839	LED
405	0.063	0.541	0.162	0.131	0.000	0.000	0.102	0.774	MH
351	0.127	0.065	0.656	0.004	0.000	0.000	0.147	0.941	HPS
44	0.014	0.109	0.643	0.006	0.000	0.049	0.178	0.886	HPS
126	0.000	0.047	0.722	0.103	0.000	0.000	0.128	0.940	HPS

In situ obs. number	Share of lamp type in *in situ* observation detailed spectral signature (unmixing results)							Max correlation between detailed signatures of *in situ* obs. and lamps	
	CFL	MH	HPS	LPS	Incand	MV	LED	Correlation	Lamp type
209	0.153	0.115	0.436	0.195	0.000	0.000	0.100	0.884	LED
398	0.061	0.321	0.159	0.057	0.079	0.000	0.323	0.890	LED
350	0.581	0.189	0.138	0.000	0.000	0.000	0.092	0.770	CFL
462	0.041	0.610	0.107	0.143	0.000	0.000	0.099	0.828	MH
241	0.230	0.039	0.151	0.000	0.000	0.484	0.096	0.671	MV
521	0.023	0.007	0.028	0.004	0.054	0.032	0.851	0.985	LED
404	0.054	0.572	0.128	0.146	0.000	0.000	0.100	0.816	MH
569	0.238	0.063	0.000	0.000	0.000	0.000	0.699	0.950	LED
352	0.052	0.058	0.148	0.000	0.005	0.000	0.737	0.976	LED
2	0.216	0.296	0.061	0.000	0.000	0.242	0.185	0.648	CFL
284	0.083	0.531	0.262	0.000	0.000	0.000	0.124	0.719	MH
447	0.035	0.515	0.283	0.131	0.011	0.000	0.025	0.802	MH
498	0.586	0.257	0.000	0.000	0.000	0.000	0.157	0.760	CFL
108	0.000	0.058	0.642	0.141	0.000	0.000	0.159	0.928	LED
196	0.064	0.098	0.577	0.132	0.000	0.000	0.129	0.925	HPS
540	0.183	0.027	0.138	0.000	0.021	0.399	0.232	0.697	LED
95	0.068	0.077	0.679	0.006	0.000	0.000	0.170	0.940	HPS
85	0.016	0.135	0.611	0.054	0.010	0.000	0.175	0.938	LED
141	0.000	0.288	0.462	0.126	0.000	0.000	0.124	0.877	HPS
113	0.041	0.482	0.234	0.189	0.025	0.000	0.028	0.838	MH
307	0.020	0.396	0.381	0.091	0.037	0.000	0.075	0.861	LED
37	0.186	0.106	0.458	0.146	0.000	0.000	0.104	0.733	LED
477	0.133	0.025	0.193	0.000	0.000	0.555	0.095	0.689	MV
476	0.133	0.026	0.200	0.000	0.000	0.549	0.091	0.686	MV
13	0.147	0.444	0.152	0.174	0.047	0.000	0.037	0.886	MH
143	0.036	0.091	0.600	0.233	0.000	0.000	0.040	0.878	HPS
542	0.181	0.027	0.139	0.000	0.033	0.391	0.230	0.701	LED
437	0.000	0.105	0.601	0.218	0.000	0.000	0.077	0.879	HPS
28	0.002	0.079	0.641	0.165	0.000	0.000	0.113	0.928	HPS
578	0.117	0.549	0.049	0.010	0.072	0.000	0.203	0.850	LED
580	0.092	0.583	0.162	0.000	0.022	0.000	0.143	0.806	LED
582	0.111	0.549	0.178	0.000	0.000	0.018	0.145	0.684	MH
541	0.174	0.029	0.127	0.000	0.035	0.371	0.264	0.755	LED
200	0.000	0.114	0.607	0.169	0.000	0.000	0.109	0.922	HPS
412	0.000	0.537	0.155	0.097	0.059	0.000	0.152	0.728	LED
268	0.006	0.016	0.261	0.000	0.008	0.000	0.710	0.990	LED
435	0.000	0.081	0.606	0.208	0.026	0.000	0.080	0.873	HPS
218	0.051	0.354	0.333	0.121	0.015	0.000	0.126	0.893	LED
561	0.000	0.103	0.373	0.200	0.230	0.000	0.095	0.826	LED
534	0.100	0.109	0.457	0.217	0.000	0.063	0.055	0.795	HPS

In situ obs. number	Share of lamp type in *in situ* observation detailed spectral signature (unmixing results)							Max correlation between detailed signatures of *in situ* obs. and lamps	
	CFL	MH	HPS	LPS	Incand	MV	LED	Correlation	Lamp type
Avg.	**0.111**	**0.220**	**0.328**	**0.088**	**0.052**	**0.044**	**0.156**		